ULTRAFAST OPTICS

Angular momentum–induced delays in solid-state photoemission enhanced by intra-atomic interactions

Fabian Siek,[1] Sergej Neb,[1] Peter Bartz,[1] Matthias Hensen,[1] Christian Strüber,[1]* Sebastian Fiechter,[2] Miquel Torrent-Sucarrat,[3,4,5] Vyacheslav M. Silkin,[3,4,5] Eugene E. Krasovskii,[3,4,5] Nikolay M. Kabachnik,[6,7] Stephan Fritzsche,[8] Ricardo Díez Muiño,[4,9] Pedro M. Echenique,[3,4,9] Andrey K. Kazansky,[3,4,5] Norbert Müller,[1] Walter Pfeiffer,[1]† Ulrich Heinzmann[1]

Attosecond time-resolved photoemission spectroscopy reveals that photoemission from solids is not yet fully understood. The relative emission delays between four photoemission channels measured for the van der Waals crystal tungsten diselenide (WSe_2) can only be explained by accounting for both propagation and intra-atomic delays. The intra-atomic delay depends on the angular momentum of the initial localized state and is determined by intra-atomic interactions. For the studied case of WSe_2, the photoemission events are time ordered with rising initial-state angular momentum. Including intra-atomic electron-electron interaction and angular momentum of the initial localized state yields excellent agreement between theory and experiment. This has required a revision of existing models for solid-state photoemission, and thus, attosecond time-resolved photoemission from solids provides important benchmarks for improved future photoemission models.

Photoemission spectroscopy is widely used to study electronic properties of solids. The momentum and energy distribution of photoelectrons reflect the electronic ground state and are well understood based on theoretically derived electronic ground-state configurations and delocalized photoemission states. However, as demonstrated here, the dynamics of the photoemission process is not correctly captured in common models of solid-state photoemission. In the very initial stage of the photoemission process, the excited-state dynamics is governed by the local environment, i.e., the inner configuration of the atom. This gives rise to an angular momentum–dependent delay that is enhanced by intra-atomic interactions (top left of Fig. 1 and supplementary materials section 2.1). These effects are well established for the photoemission from atoms (*1*–*4*) but are neglected in models of solid-state photoemission. Realistic modeling of photoelectron kinematics and photoemission delays thus requires a revision of these models, i.e., both intra-atomic delays and propagation effects must be considered (Fig. 1, top).

The reported results are based on attosecond time-resolved photoemission spectroscopy using the streaking approach (*5*). As depicted in Fig. 1, the photoelectron excited by an attosecond extreme ultraviolet (EUV) pulse is exposed to an infrared (IR) streaking field. The delay $t_{IR} - t_{EUV}$ between the IR and EUV pulses and the photoemission delay, i.e., the time until the photoelectron leaves the solid and feels the streaking field, determine the streaking signal (*5*), and the streaking spectrogram yields delay differences between the various emission channels. WSe_2 is chosen as the substrate because the photoemission spectrum for the EUV photon energy (Fig. 2A) is dominated by four emission channels with different initial-state characteristics: a valence band (VB) emission (E_{kin} = 87.0 eV) and photoemission from the Se 4s, W 4f, and Se 3d core levels at E_{kin} = 73.5 eV, E_{kin} = 54.2 eV, and E_{kin} = 32.2 eV (*6*), respectively. WSe_2 (Fig. 1) allows in situ cleaving and yields rather inert surfaces. Its layered structure helps identify the depth from which a particular photoelectron is emitted. Together with the minimization of systematic errors induced by the chirp of the EUV pulse (<0.01 fs^2) and magnetic fields (<1 μT) to less than 2 as, this procedure allows us to determine the relative photoemission delays with 10-as resolution.

From fitting the background-corrected spectra recorded for different delay $t_{IR} - t_{EUV}$, the delay-dependent energy positions of four spectral components were determined (Fig. 2B). Simultaneous fitting (continuous lines in the overlay in Fig. 2B) of these streaking curves yields the photoemission delays Δt and the corresponding relative photoemission delays $\Delta t_{VB-Se4s}$, $\Delta t_{Se3d-Se4s}$, and $\Delta t_{W4f-Se4s}$ relative to the emission from the Se 4s core level. The latter are shown on the left side of Fig. 3 as a function of time after cleaving. Within the experimental uncertainties, the delays show no systematic variation. Consequently, the individual measurements are averaged, and small statistical uncertainties of ~10 as are achieved for the three different relative delays (red data points in the right side of Fig. 3). Averaging over different subensembles (see supplementary materials section 1.3 for details) does not significantly alter the retrieved average relative delays. In addition, ambiguities in the delay determination arising from various data evaluation procedures are excluded. Five different background subtraction procedures (see fig. S1B) yield, within the statistical uncertainty, the same relative delays (right side of Fig. 3). As systematic errors are negligible, the error margins for the experimentally determined photoemission delays noted in the right side of Fig. 3 and tabulated in Table 1 reflect the counting statistics of individual streaking spectra, scattering of results for different WSe_2 crystals, different positions on the cleaved surfaces, and ambiguities of the evaluation procedure.

The positive relative delays indicate a photoemission sequence as follows: The photoelectrons emitted from the Se 4s state arrive first, then, about 10 as later, the electrons from the VB ($\Delta t_{VB-Se4s}$ = 12 ± 10 as) arrive, and roughly an additional 15 as later, photoelectrons originating from the Se 3d core level appear ($\Delta t_{Se3d-Se4s}$ = 28 ± 10 as). Finally, the electrons from the W 4f state arrive about 20 as later ($\Delta t_{W4f-Se4s}$ = 47 ± 14 as) than the Se 3d photoelectrons. This emission sequence has a striking qualitative behavior: The emission events appear time ordered with respect to rising angular momentum of the initial states. Emission from Se 4s is fastest, although the kinetic energy of the photoelectrons is lower than for the VB emission and is thus expected to proceed slower. The emission from the state with the highest angular momentum, i.e., the W 4f state, arrives last. Electrons originating from Se 3d have a lower kinetic energy than those originated from the W 4f state but are emitted earlier. Assignment of an angular momentum to the VB is difficult, but the bonding in WSe_2 is dominated by Se 4p and W 5d orbitals (supplementary material section 2.2), and thus the VB emission also matches this pattern of increasing delay with increasing angular momentum. This time ordering according to initial-state angular momenta provides a first hint that intra-atomic effects (Fig. 1) affect the photoemission kinematics. However, the effects are subtle, and a theoretical analysis accounting for known effects that influence the photoemission delay is needed to clearly identify the underlying mechanisms.

Table 1 summarizes the measured delays and compares them to theory. A full three-dimensional quantum mechanical model that accounts for the transient many-body effects is still beyond the reach of the contemporary theoretical methods. Here we separate the photoemission process into two steps, i.e., an intra-atomic initial stage and the propagation in an effective one-dimensional

[1]Fakultät für Physik, Universität Bielefeld, Universitätsstr. 25, 33615 Bielefeld, Germany. [2]Institut für Solare Brennstoffe, Helmholtz-Zentrum Berlin für Materialien und Energie GmbH, Hahn-Meitner-Platz 1, 14109 Berlin, Germany. [3]University of the Basque Country, 20080 San Sebastián, Spain. [4]Donostia International Physics Center, 20018 San Sebastián, Spain. [5]IKERBASQUE, Basque Foundation for Science, 48013 Bilbao, Spain. [6]Skobeltsyn Institute of Nuclear Physics, Lomonosov Moscow State University, Moscow 119991, Russia. [7]European XFEL GmbH, Holzkoppel 4, 22869 Schenefeld, Germany. [8]Helmholtz-Institut Jena, Fröbelstieg 3, 07743 Jena, Germany. [9]Centro de Física de Materiales CFM/MPC (CSIC-UPV/EHU), 20018 San Sebastián, Spain.
*Present address: Max Born Institute for Nonlinear Optics and Short Pulse Spectroscopy in the Forschungsverbund Berlin e.V., Max-Born-Straße 2 A, 12489 Berlin, Germany. †**Corresponding author. Email: pfeiffer@physik.uni-bielefeld.de**

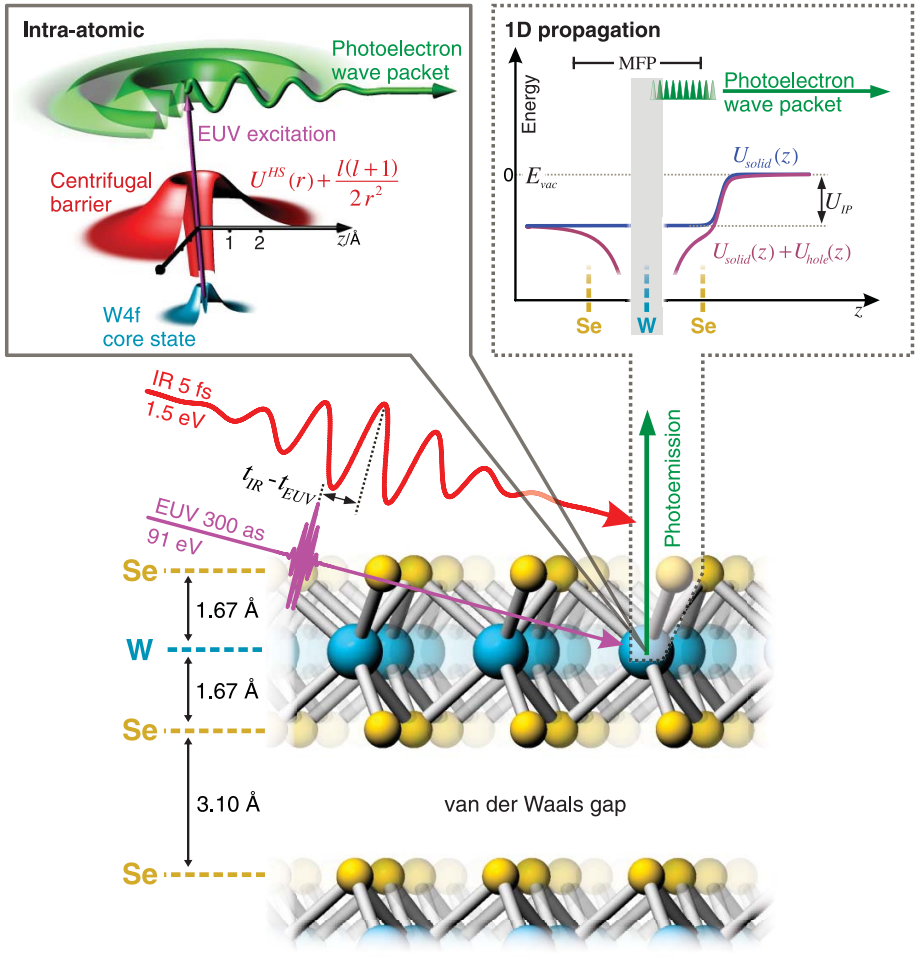

Fig. 1. Elementary steps in photoemission from the van der Waals crystal WSe_2. The WSe_2 substrate and the principle of attosecond time-resolved streaking spectroscopy are depicted. The surface held at room temperature is illuminated collinearly with a 300-as long EUV pulse with 91-eV center energy and an intense few-cycle IR streaking field (85° angle of incidence, p-polarized). The EUV pulses excite photoelectrons (here shown for the W 4f photoemission) that are then streaked in the IR field, i.e., are gaining or losing kinetic energy depending on the delay $t_{IR} - t_{EUV}$ between the EUV and IR pulses. As indicated in the upper left panel, the initial stage of photoemission is dominated by intra-atomic processes: Within the HS approach, the photoelectron wave (green) created by EUV excitation from the W 4f state (blue) is governed by the effective radial potential (red) composed of the HS potential U^{HS} and the centrifugal term. The wave packet propagation in the later stage is schematically depicted in the right panel. It is dominated by a 1D potential that accounts for the inner potential U_{IP} of WSe_2 and the interaction with the remaining photohole. The inelastic MFP for the photoelectron is indicated as a horizontal bar and E_{vac} indicates the position of the vacuum energy.

(1D) potential in the solid, shown at the top of Fig. 1.

The intra-atomic delays summarized in Table 1 are derived by using both an independent-electron Hartree-Slater (HS) model (*7*) and the multiconfiguration Dirac-Fock (MCDF) approach (*8*), which accounts for electron correlations and relativistic effects (supplementary materials section 2.1). Both methods consistently yield relative delays that become larger as the difference in angular momentum from the Se 4s state increases. In contrast to the MCDF calculations, the HS method provides an intuitive interpretation of the intra-atomic effects enhancing the photoemission delays (top left of Fig. 1 and supplementary materials section 2.1.3): The electron-electron interaction within the atom screens the Coulomb interaction with the nucleus and is taken into account in a single-particle approach by the spherically symmetric HS potential $U^{HS}(r)$. The effective potential $U_{eff}^{HS}(r) = U^{HS}(r) + l(l+1)/2r^2$ (in atomic units, where r is the radial distance to the atomic nucleus and l is the angular momentum) that combines electrostatic attraction and centrifugal repulsion governs the photoelectron dynamics. In time-resolved experiments performed on atoms (*2*) and molecules (*9*), this mechanism is well established and accounted for in theoretical modeling of photoemission delays (*4*). For high angular momenta $l \geq 2$, the complicated shape of the effective potential strongly varies with atomic number Z (*10*). Such an l-dependent effective potential determines the photoelectron phase shift (and time delay), which includes the impact of intra-atomic interactions. Accordingly, the time delay depends on l and thus on the electron angular momentum in the initial atomic state (see supplementary materials section 2.1). The impact of the centrifugal term increases with an increase of l and is most pronounced in the core of the atom where charge screening is most effective, i.e., for radii smaller than about 1 Å. Thus, the corresponding delay is accumulated in the very initial stage of the photoemission process. This strong localization allows for the separation of the photoemission process into an intra-atomic initial step and the subsequent propagation in the solid.

Table 1. Comparison between experimental and theoretical photoemission delays. The second column specifies the difference between the kinetic energies for X and Se 4s photoelectrons. The third column summarizes the experimental delays as indicated in Fig. 3. The fourth column lists the summed intra-atomic and propagation-induced delays derived by using either the HS or the MCDF approach (fifth column) and 1D TDSE simulation of propagation in the solid (sixth column), respectively. The values derived using the MCDF approach are indicated in squared brackets. For details, see supplementary materials section 2.

X	$E_{kin}^{X} - E_{kin}^{Se4s}$ (eV)	Experimental Δt_{X-Se4s} (as)	Theory Σ total including HS or MCDF (as)	Atomic delay HS or MCDF (as)	Propagation delay 1D TDSE (as)
VB 4p/5d	13.5	12 ± 10	12 [12]	6 [6]	6
Se 3d	–41.3	28 ± 10	29 [25]	14 [10]	15
W 4f	–19.3	47 ± 14	44 [36]	20 [12]	24

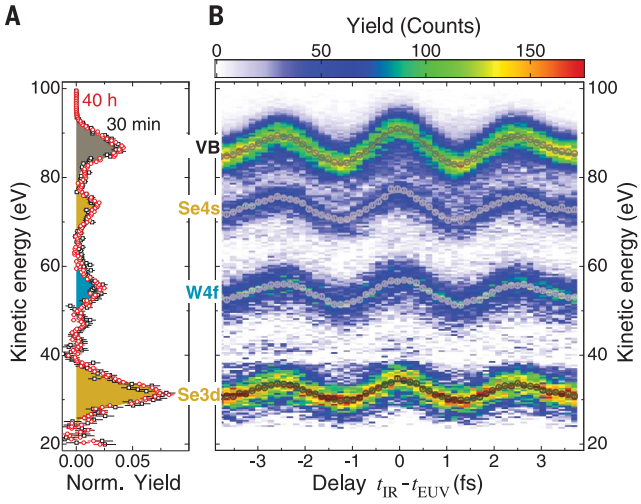

Fig. 2. Attosecond time-resolved photoemission spectroscopy from WSe_2. (**A**) Long-term stability of the surface over 40 hours. Background-corrected photoemission spectra (fig. S1A) recorded 30 min (black circles) and 40 hours (red circles) after cleaving. The photoelectron peaks for VB, Se 4s, W 4f, and Se 3d are indicated. The spectra are normalized to the total yield after background subtraction. (**B**) Streaking spectrogram. As a function of the delay between the IR and EUV pulses, the photoemission spectra (after background subtraction) are shown as a density plot. For each delay, the energy positions (overlaid symbols) of the VB, Se 4s, W 4f, and Se 3d emissions and the corresponding simultaneously fitted IR field-time dependence (eq. S1) yielding the delay parameters Δt for each emission channel (continuous overlaid lines) are shown.

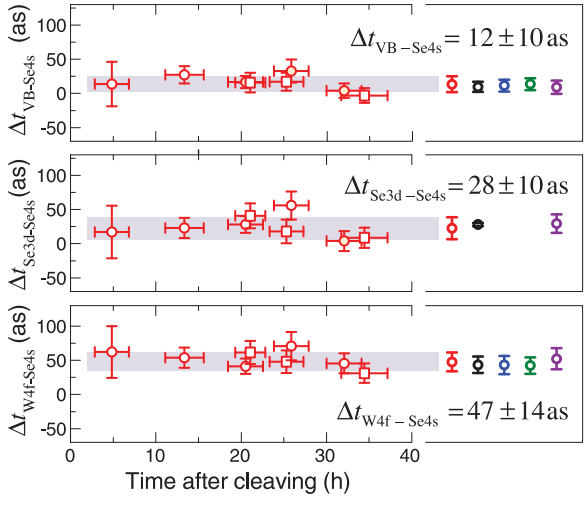

Fig. 3. Relative photoemission delays. The left side shows the relative photoemission delays $\Delta t_{VB-Se4s}$, $\Delta t_{Se3d-Se4s}$, and $\Delta t_{W4f-Se4s}$ as a function of time after cleaving for two different crystals indicated by different symbols (circles and squares) using the background subtraction method based on a model spectrum (fig. S1A). The horizontal error bars indicate the time period during which the spectrogram was recorded, and the vertical bars indicate the uncertainty of the delay determination. On the right, the average delays obtained by various background-subtraction procedures are shown: background based on model spectrum (red circle), parabolic background (black circle), combination of parabolic and Shirley background with and without delay-dependent background (blue and green circles, respectively), and delay-dependent background based on model spectrum (magenta circle).

The photoelectron propagation in the solid and the emission are modeled by using a single-particle time-dependent Schrödinger equation approach (TDSE) (*11*, *12*). The method originally developed for gas-phase streaking (*13*) is adapted here to account for the streaking field distribution, the inner potential of WSe_2 (*14*), inelastic electron scattering in the solid, and the photoelectron-photohole interaction. For normal emission, the streaking is determined by the normal component of the IR field. For this reason, the TDSE can be restricted to propagation in one dimension. The dynamical screening and penetration of the IR field (fig. S5) and the inelastic mean free path (MFP) (fig. S6) are derived from ab initio electronic structure calculations for WSe_2 (supplementary materials sections 2.2.3 and 2.2.4). For each atomic layer and initial state, the streaking spectrograms are calculated separately and then added, yielding the total streaking spectrogram as incoherent superposition of the different emission channels (fig. S9) and the corresponding photoemission delays listed in Table 1. This approach incorporates all previously demonstrated photoemission delay mechanisms that were identified based on various approaches (*11*, *12*, *15*–*23*): wave packet propagation (*24*–*27*), inelastic scattering in the bulk solid (*21*, *28*), initial-states localization (*19*), and a realistic choice of the "streaking clock" position, i.e., the position along the photoelectron trajectory at which the electron starts to be exposed to the streaking field (*21*, *25*).

Compared to the experimental values, the delays obtained by using the 1D TDSE propagation alone (Table 1, column 1D TDSE) are systematically too small by about a factor two. This discrepancy is robust with respect to realistic variations of the MFP (4 to 5 Å), the electron-hole (e-h)–interaction screening length, and the exact position of the attosecond clock (±0.5 Å). Neither atomic delays nor propagation effects alone account for the experimentally observed delays. However, if propagation-induced delays and atomic delays are joined, the total delay (column "Theory Σ" in Table 1) matches the experimental observations. On the basis of this, we conclude that the angular momentum of the initial localized atomic state affects the time delay of photoelectrons in solids. Intra-atomic interactions substantially contribute to the total delay.

This observation is in contrast to state-of-the-art photoemission models that emphasize the translational invariance in the solid for the initial and excited states. As demonstrated, the initially excited localized wave packet is dominated by the spherical symmetry of the atom from which the electron is emitted. Only after some time, as the wave propagates to neighboring atoms, does the photoelectron feel the structure of the crystal. This complex evolution of a many-body system is not captured in common photoemission models, and attosecond time-resolved photoemission spectroscopy thus provides access to investigating this initial phase of the photoemission process in more detail. Incorporating this initial stage, which is localized at the particular atom from which the electron is emitted, is the cornerstone of our model and any future models of solid-state photoemission.

REFERENCES AND NOTES

1. M. Schultze *et al.*, *Science* **328**, 1658–1662 (2010).
2. K. Klünder *et al.*, *Phys. Rev. Lett.* **106**, 143002 (2011).
3. M. Ossiander *et al.*, *Nat. Phys.* **13**, 280–285 (2016).
4. R. Pazourek, S. Nagele, J. Burgdörfer, *Rev. Mod. Phys.* **87**, 765–802 (2015).
5. A. L. Cavalieri *et al.*, *Nature* **449**, 1029–1032 (2007).
6. A. Klein *et al.*, *Sol. Energy Mater. Sol. Cells* **51**, 181–191 (1998).
7. F. Herman, S. Skillman, *Atomic Structure Calculations* (Prentice-Hall, 1963).
8. I. P. Grant, in *Methods in Computational Chemistry* (Plenum Press, New York, 1988), vol. 2, pp. 1–71.
9. M. Huppert, I. Jordan, D. Baykusheva, A. von Conta, H. J. Wörner, *Phys. Rev. Lett.* **117**, 093001 (2016).
10. U. Fano, J. W. Cooper, *Rev. Mod. Phys.* **40**, 441–507 (1968).
11. A. K. Kazansky, P. M. Echenique, *Phys. Rev. Lett.* **102**, 177401 (2009).
12. A. G. Borisov, D. Sánchez-Portal, A. K. Kazansky, P. M. Echenique, *Phys. Rev. B* **87**, 121110 (2013).
13. A. K. Kazansky, N. M. Kabachnik, *J. Phys. At. Mol. Opt. Phys.* **40**, 2163–2177 (2007).
14. T. Finteis *et al.*, *Phys. Rev. B* **55**, 10400–10411 (1997).
15. C. Lemell, B. Solleder, K. Tőkési, J. Burgdörfer, *Phys. Rev. A* **79**, 062901 (2009).
16. J. C. Baggesen, L. B. Madsen, *Phys. Rev. A* **78**, 032903 (2008).
17. E. E. Krasovskii, *Phys. Rev. B* **84**, 195106 (2011).
18. S. Nagele *et al.*, *J. Phys. At. Mol. Opt. Phys.* **44**, 081001 (2011).
19. C.-H. Zhang, U. Thumm, *Phys. Rev. A* **84**, 065403 (2011).
20. C.-H. Zhang, U. Thumm, *Phys. Rev. A* **84**, 063403 (2011).
21. Q. Liao, U. Thumm, *Phys. Rev. A* **89**, 033849 (2014).
22. Q. Liao, U. Thumm, *Phys. Rev. Lett.* **112**, 023602 (2014).

23. U. Heinzmann, in *Attosecond Physics*, L. Plaja, R. Torres, A. Zaïr, Eds. (Springer Series in Optical Sciences, Springer Berlin Heidelberg, 2013), pp. 231–253.
24. S. Neppl *et al*., *Phys. Rev. Lett.* **109**, 087401 (2012).
25. S. Neppl *et al*., *Nature* **517**, 342–346 (2015).
26. R. Locher *et al*., *Optica* **2**, 405 (2015).
27. Z. Tao *et al*., *Science* **353**, 62–67 (2016).
28. I. Nagy, P. M. Echenique, *Phys. Rev. B* **85**, 115131 (2012).

ACKNOWLEDGMENTS

This work was supported by the German Research Foundation (DFG) within the Collaborative Research Center (SFB) 613 (F.S., P.B., W.P., and U.H.), the Priority Programs SPP 1931 (C.S., M.H., and W.P.), and SPP 1840 (St.F., S.N., and W.P.); the Basque Government (grant IT-756-13 UPV/EHU) (V.M.S., E.E.K., R.D.M., P.M.E., and A.K.K.); and the Spanish Ministerio de Economía y Competitividad (grants FIS2016-76617-P and FIS2016-76471-P) (V.M.S., E.E.K., R.D.M., P.M.E., and A.K.K.) and Fondo Europeo de Desarrollo Regional (FEDER) (CTQ2016-80375-P) (M.T.-S.). N.M.K. acknowledges hospitality and financial support from the theory group in cooperation with the small quantum systems (SQS) research group of European XFEL. All data needed to evaluate the conclusions in this study are presented in the paper and/or in the supplementary materials. Additional data related to this study may be requested from W.P. (pfeiffer@physik.uni-bielefeld.de). F.S. and S.N. performed the experiments. F.S., S.N., P.B., M.H., C.S., and N.M. contributed to the development and operation of the experimental setup and Se.F. provided the WSe_2 crystals and supervised in situ preparation. F.S., S.N., and W.P. analyzed the experimental results. A.K.K. developed the 1D TDSE propagation model and coordinated the various theoretical activities concerned with intra-atomic delays (A.K.K., St.F., and N.M.K.), electron MFP in WSe_2 and the dynamically IR streaking-field distribution at the WSe_2-vacuum interface (V.M.S. and R.D.M.), effective mass of photoelectrons in WSe_2 (E.E.K.), and the projected initial states (M.T.-S.). P.M.E., U.H., and W.P. supervised the project.

SUPPLEMENTARY MATERIALS

www.sciencemag.org/content/357/6357/1274/suppl/DC1
Materials and Methods
Figs. S1 to S9
Tables S1 to S3
References (*29*–*72*)

28 April 2017; accepted 11 August 2017
10.1126/science.aam9598

Angular momentum–induced delays in solid-state photoemission enhanced by intra-atomic interactions

Fabian Siek, Sergej Neb, Peter Bartz, Matthias Hensen, Christian Strüber, Sebastian Fiechter, Miquel Torrent-Sucarrat, Vyacheslav M. Silkin, Eugene E. Krasovskii, Nikolay M. Kabachnik, Stephan Fritzsche, Ricardo Díez Muiño, Pedro M. Echenique, Andrey K. Kazansky, Norbert Müller, Walter Pfeiffer and Ulrich Heinzmann

Science **357** (6357), 1274-1277.
DOI: 10.1126/science.aam9598

Photoemission with a twist

Attosecond time-resolved spectroscopy provides the ability to probe the fastest electronic processes in atoms and solids. Yet the photoemission process from solids is not fully understood. Siek *et al.* studied photoemission from the layered van der Waals material WSe_2 and found that electron emission occurs as a sequence of events that are apparently time-ordered with respect to rising angular momentum of the involved initial states (see the Perspective by Yakovlev and Karpowicz). This result will help provide a more detailed picture of the photoemission process.

Science, this issue p. 1274; see also p. 1239